In situ electron paramagnetic resonance correlated spectroscopy and imaging: a tool for lithium-ion batteries to investigate metallic lithium sub-micrometric structures created by plating and stripping

Charles-Emmanuel Dutoit[1,2,*,†], Mingxue Tang[1,2,‡], Didier Gourier[3], Jean-Marie Tarascon[2,4], Hervé Vezin[5,*] & Elodie Salager[1,2]

[1]*CNRS, CEMHTI UPR3079, Université d'Orléans, 45071 Orléans, France*

[2]*Réseau sur le Stockage Electrochimique de l'Energie (RS2E), FR CNRS 3459, France*

[3]*Chimie-ParisTech, PSL Université, CNRS, Institut de Recherche de Chimie-Paris (IRCP), 75005 Paris, France*

[4]*Collège de France, CNRS FRE3357, 75005 Paris, France*

[5]*Université Lille Nord de France, CNRS UMR8516, LASIR, 59655 Villeneuve d'Ascq, France*

Monitoring the formation of dendrites or filaments of lithium is of paramount importance for Li-based battery technologies, hence the intense activities in designing *in situ* techniques to visualize their growth. Herein we report the benefit of correlating *in situ* electron paramagnetic resonance (EPR) spectroscopy and EPR imaging to analyze the morphology and location of metallic lithium in a symmetric Li/LiPF$_6$/Li electrochemical cell during polarization. We exploit the variations in shape, resonance field and amplitude of the EPR spectra to follow, *operando*, the nucleation of sub-micrometric Li particles (narrow and symmetrical

---

[†]Present address: Chimie-ParisTech, PSL Université, CNRS, Institut de Recherche de Chimie-Paris (IRCP), Paris, France
[‡]Present address: Center for high pressure science and technology advanced research, Beijing, China

signal) that conjointly occurs with the fragmentation of bulk Li on the opposite electrode (asymmetrical signal). Moreover, *in situ* EPR correlated spectroscopy and imaging (spectral-spatial EPR imaging) allows the identification (spectral) and localization (spatial) of the sub-micrometric Li particles created by plating (deposition) or stripping (altered bulk Li surface). We finally demonstrate the possibility to visualize, via *in situ* EPR imaging, dendrites formed through the separator in the whole cell. Such a technique could be of great help in mastering the Li-electrolyte interface issues that plague the development of solid-state batteries.

Introduction

Rechargeable lithium-ion batteries (LIBs) are recognized for the good balance between weight, volume and electrochemical performance. Despite the wide range of applications for LIBs, prevention of non-uniform deposition of metallic lithium is still of paramount importance to avoid internal short-circuits and thermal runaway. Formation of lithium dendrites on the negative graphitic electrode is an issue in mature LIBs that prevents faster charge, essential for the development of transport electrification,[1,2] while lithium filament growth hinders the spread of all-solid-state batteries.[3,4]

Metallic lithium deposition in batteries is still relatively hard to predict, and the visualization, in real time, of its location, morphology and growth is the subject of intense development for many techniques.[5] A precious feature of Electron Paramagnetic Resonance (EPR) is the combination of imaging and spectroscopy, unexplored to date for the characterization of lithium deposition in batteries. In 2015 *in situ* EPR was demonstrated as a tool of choice to detect Li deposits, either

by imaging[6] or spectroscopy.[7] In continuation of the latter an extensive study by *operando* EPR spectroscopy was performed for Li plating on graphite.[8] Niemöller et al. also studied, *ex situ*, the potential and limitations of *ex situ* EPR imaging (EPRI) on metallic Li [9].

In this paper, we report the combination of *in situ* X-band EPR spectroscopy and imaging to observe directly, *in situ*, the morphology and the distribution of metallic lithium in a symmetric Li/LiPF$_6$/Li electrochemical cell. We observe the roughening of the lithium surface upon stripping, the spatially inhomegeneous electrodeposition of the sub-micrometric lithium particles and dendrite growth causing a short-circuit.

Results and discussion

Figure 1a shows a schematic representation of the Li/LiPF$_6$/Li electrochemical cell placed in the EPR resonator, with the static magnetic field **H** oriented along the **Z** axis and the microwave field along the **Y** axis. The magnetic field gradients, used for imaging, are oriented along the **Y** and **Z** axes. This configuration is optimized to study lithium exchange between the two electrodes and especially dendritic growth. The EPR spectrum of the assembled electrochemical cell in the pristine state, before applying the current flow, is shown in fig. 1c. It is identical to the spectrum of a metallic lithium disk (fig. 1b), as expected. The resonance field and therefore the measured g factor (g=2.0030, close to the free electron spin g=2.0023) is characteristic of metallic lithium.

Previous EPR investigations showed that the lineshape, linewidth and intensity were highly dependent on the morphology of metallic lithium. [6,7,9] The EPR spectrum lineshape of a metallic
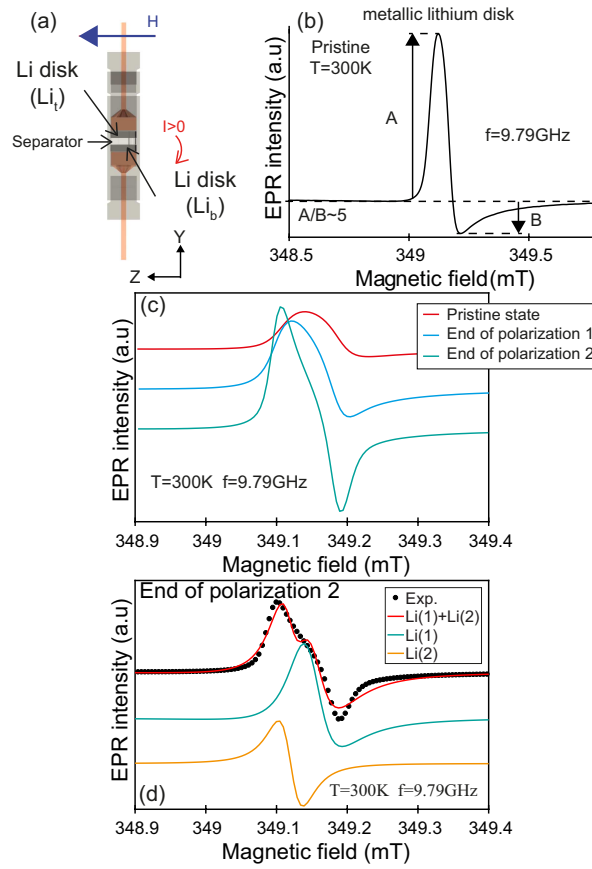
Figure 1: *Operando* EPR spectroscopy recorded at 9.79 GHz. (a) Schematic representation of the EPR electrochemical cell and its orientation in the external magnetic field **H**. **Y** and **Z** are the magnetic field gradient directions for imaging. (b) cw-EPR spectrum of a pristine metallic lithium disk (no cycling). A and B denote the amplitude of the positive and negative parts of the EPR line respectively. (c) Selection of *operando* cw-EPR spectra of the Li/LiPF$_6$/Li cell. A symmetrical and sharp EPR line appears in the low magnetic field flank of the bulk signal upon polarization. (d) Experimental (black dots) and simulated (red line) EPR spectra at the end of polarization 2. The dysonian component of the simulation Li(1) is assigned to the bulk Li signal of both electrodes and the lorentzian component Li(2) to the newly formed sub-micrometric Li particles.
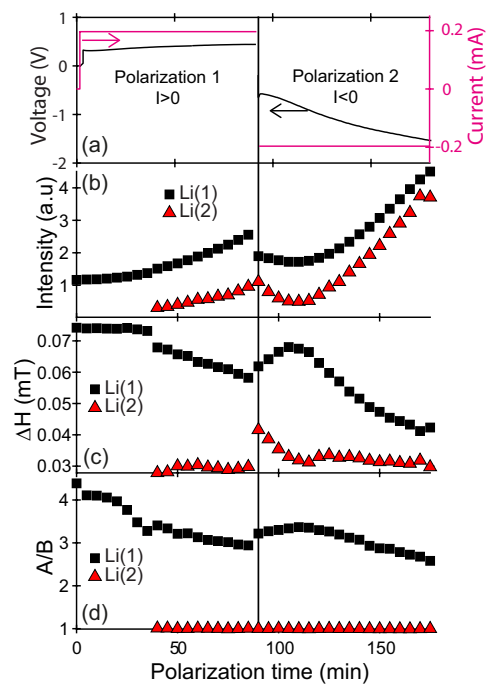
Figure 2: Evolution of the cw-EPR parameters versus polarization time for the two components, Li(1) (bulk Li) and Li(2) (micrometric particles). (a) Voltage (left) and current (right) of the electrochemical cell, (b) EPR spectrum intensity, (c) linewidth ΔH and (d) asymmetry ratio A/B.

47 conductor is indeed controlled by the limited penetration depth δ_{mw} of the microwave field in the

48 metal, known as the skin effect: [10]

$$\delta_{mw} \propto \sqrt{\frac{\rho}{f}} \qquad (1)$$

49   ρ being the metal resistivity and f the microwave frequency.

50   More precisely the EPR spectrum lineshape depends on the metal thickness d compared

51 to δ_{mw}. If $d > \delta_{mw}$, only the spins located inside the skin depth are excited by the microwave

52 field. During the spin coherence time T_2, each electron travels on a distance of the order of

53 $\delta_{eff} \approx (D_e T_2)^{\frac{1}{2}}$ where D_e is the diffusion coefficient of electrons.[10,11] As $\delta_{eff} \approx 60\mu m$ in metal-

54 lic lithium,[9] the electrons penetrate several times in the skin region during T_2 ($\sim 10^{-9}$ sec), and

55 thus experience each time a microwave pulse, resulting in an asymmetrical (dysonian) lineshape

56 classically characterized by the asymmetry ratio A/B≈5. [10,11] If $d < \delta_{mw}$, all the electronic spins

57 experience the same microwave field, resulting in a symmetrical Lorentzian EPR line. Conse-

58 quently the presence of sub-micrometric metallic lithium such as dendritic and/or mossy structures

59 can be revealed by the shape of the EPR spectrum. As expected for a Li electrode in the pristine

60 state (fig.1b), a single dysonian lineshape with A/B≈5 is observed, typical of thick metal. This is

61 in good agreement with the thickness d=400 μm of the Li electrode, which is much larger than the

62 skin depth $\delta_{mw} \approx$1 μm for Li at 9.6 GHz.[6,7]

63   The Li//Li cell was polarized to follow the mechanisms of Li stripping and plating with a

current density of 1 mA/cm^2 (fig. 2a). During polarization 1, the top Li electrode is oxidized (Li

stripping) and the bottom electrode is reduced (Li electroplating). In polarization 2 this process is

reversed. No sign of cell failure was observed after 175 min of positive and negative polarization.

Three spectra of the cell, corresponding to the pristine state (t=0 min), the end of polarization

1 (t=85 min) and the end of polarization 2 (t=175 min), are shown in fig.1c. Between the two

polarization steps, the cell was left in open circuit (OCV) to record *in situ* EPR images. In contrast,

EPR spectra were recorded *operando* during the polarization steps, that is with current flowing

through the cell. The spectra exhibit different lineshapes, indicative of a modification of the Li

electrode morphologies upon polarization. The growth of a narrow and symmetric line in the

low field flank of the bulk Li signal results in a splitting of the EPR spectrum (fig. 1c). Each

EPR spectrum was simulated by the sum of two contributions: (i) a dysonian line for bulk Li

(Li(1)) with an asymmetry ratio 4>A/B>2, a fixed resonance field H$_{res}$=349.15 mT and a varying

linewidth ΔH; (ii) a narrow (ΔH$\sim$0.03-0.4 mT) and symmetric (A/B$\sim$1) lorentzian line (Li(2))

with resonance field H$_{res}$=349.12 mT (corresponding to g=2.0032), lower than for bulk lithium.

This new EPR line is assigned to Li particles with size d <1 μm, as discussed above. An example

of simulation is given in fig. 1d. The evolution of the EPR spectrum parameters for the two Li

species (intensity, linewidth ΔH and asymmetry A/B) during cell operation are given in fig. 2. The

intensities of the simulated lines continuously increase as the cell is polarized, to reach a factor 4

at the end of polarization 2 (t=175 min), as shown in fig. 2b. This increase in the EPR intensity

is assigned to the growth of sub-micrometric Li particles (Li(2)) on both electrodes but also to the

increased intensity of the EPR line of bulk Li (Li(1)). The latter should not be misinterpreted as

7

an increase in the total quantity of metallic Li during polarization. This increased intensity of bulk Li signal (Li(1)) is the direct consequence of the progressive decrease of the asymmetry ratio A/B from 5 to less than 3 at the end of polarization 2 (fig. 2d). This feature is the manifestation of the alteration of the two bulk electrode surfaces during cycling, which creates Li structures with size approaching the skin depth δ_{mw}. As only electron spins in the volume of the skin are responsible for the EPR signal, the roughening of bulk lithium at constant total volume of metal induces an increase of the skin volume, and thus an increase of the EPR intensity. The decrease of ΔH (fig. 2c) for bulk lithium during polarization is also the consequence of the progressive decrease of A/B for the bulk Li signal.

This evolution of the EPR signal during cell cycling indicates that the reaction $Li^0 \rightarrow Li^+$ + e^- (1) at one electrode and the reverse reaction $Li^+ + e^- \rightarrow Li^0$ (2) at the other electrode are not equivalent. In polarization 1, newly formed sub-micrometric Li particles are produced on the bottom electrode (Li_b) with reaction (2), while the progressive roughening of the bulk Li electrode on top (Li_t) occurs through reaction (1). It seems, however, that there is a beginning of reversible behaviour in the first few minutes of polarization 2, when the current is reversed, with a decrease in EPR intensity of both types of lithium, as well an increase of the A/B ratio and the linewidth ΔH of bulk lithium (fig. 2). This could indicate that the previously-formed Li microparticles on Li_b are partially consumed by reaction (1) and/or structures of lithium in electrode Li_t are fused together into larger structures through reaction (2). In the second part of polarization 2, however, the general evolution observed during polarization 1 continues, with an increase in the EPR intensities of both Li types, and a decrease of A/B and ΔH of bulk lithium (fig. 2). This

8

demonstrates the high sensitivity of *in situ* EPR spectroscopy to the nucleation of very small Li

particles and the roughening of bulk Li electrodes, and places it as a tool of choice for studying the

effect of prolonged cycling.

Interestingly, the resonance field H_{res} of EPR line for the sub-micrometric Li particles is

shifted to low field by 0.03 mT compared to the bulk Li signal. Although the nature of this shift

requires further studies, it is likely that it is produced by the dynamic nuclear polarization of

metallic lithium particles via the Overhauser effect: [12–14] the partial saturation of the EPR line po-

larizes the nuclear spins, which create a very small nuclear field H_{nuc} of around 0.03 mT, adding

to the external field H_0. As the spins resonate in the effective field $H_{eff}=H_0+H_{nuc}>H_0$, the res-

onance condition, hf=$g\mu_B$($H_{res}+H_{nuc}$) requires that H_{res} decreases when H_{nuc} increases. This

effect is maximum when the electron spins "experience" all the nuclear spins, as in the case of

the sub-micrometric Li particles. A recent NMR investigation showed that Dynamic Nuclear Po-

larization (DNP) of metallic lithium was a powerful technique for characterizing electrodeposited

microstructures.[15]

In summary, the surface of the stripped Li electrode roughens during electrochemical po-

larization, with structures of micrometric size or slightly larger, and new Li particles of sub-

micrometric size nucleate through electroplating on the opposite electrode. In order to visualize

and locate these two types of metallic Li in the electrochemical cell, we performed *in situ* electron

paramagnetic resonance imaging (EPRI) of the full cell (fig. 3a, b, c). EPR images were recorded

in the pristine state, at the end of polarization1 and of polarization 2, in open-circuit phases to
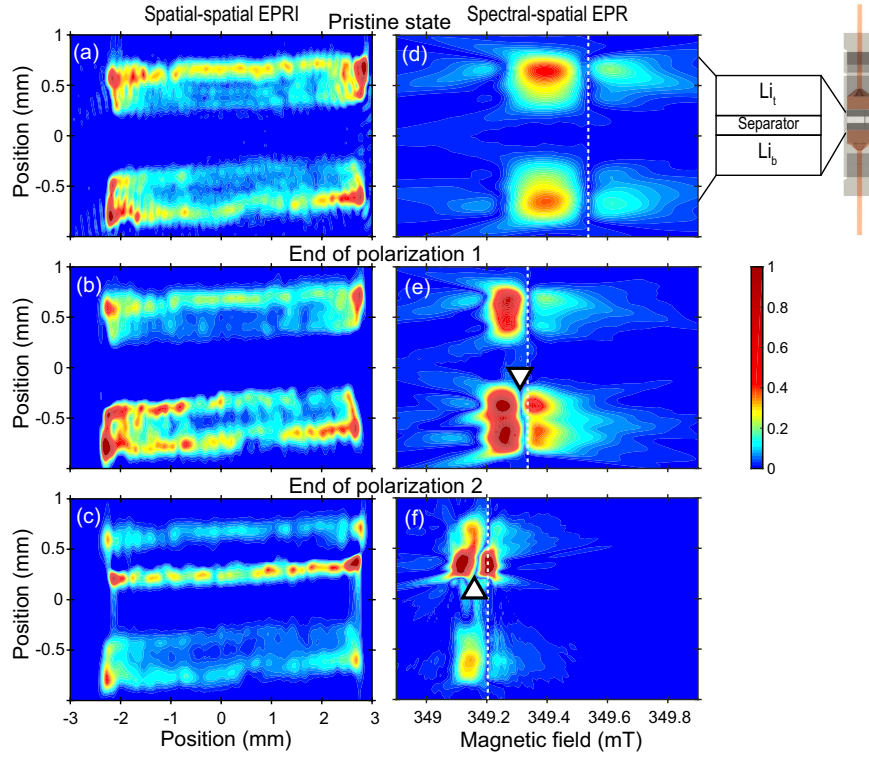
Figure 3: *In situ* X-band EPR spatial-spatial images (left) and spectral-spatial images (right) of the cell in the pristine state (top), at the end of polarization 1 (middle) and at the end of polarization 2 (bottom). The images display the absolute value of the EPR line $|d\chi''/dH|$. The vertical dashed line indicates the resonance field of the bulk Li signal and the white triangle the resonance field of the sharper component (guides to the eye). The field of the vertical dashed line shifts between spectral-spatial EPR images due to a change of the microwave frequency. The color bar indicates the color code for the intensities, identical for all plots.
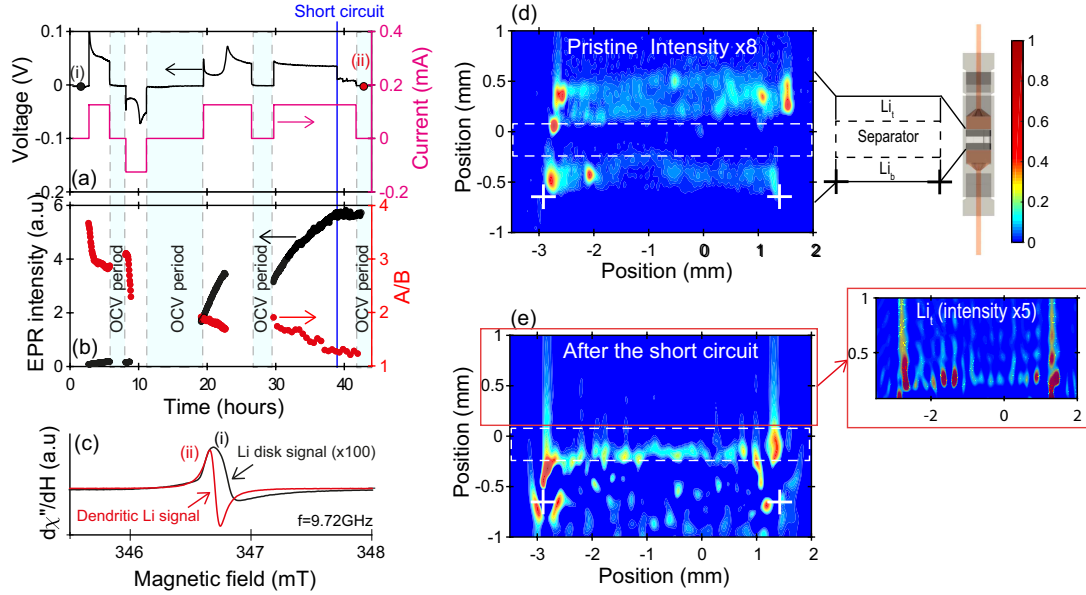
Figure 4: *In situ* detection (EPR spectrum) and localization (EPR 2D images) of dendritic Li . (a) Voltage and current of the electrochemical cell versus time. The vertical blue line indicates the short circuit with a voltage drop to 0 V and current still flowing in the cell. (b) *Operando* intensity and A/B ratio measured on the entire EPR signal (no simulation) as a function of time. (c) EPR spectra of the cell recorded in the pristine state (bulk Li electrodes) and after the short circuit (dendritic Li). The resonance field is H_{res}=346.82 mT for the bulk Li signal and H_{res}=346.7 mT for the dendritic Li signal. (d, e) *In situ* spatial-spatial EPR images recorded in the pristine state (intensity x8) and after the short circuit, respectively. Spots crossing the separator after the short circuit suggest the location of dendritic Li. The inset shows a zoom in the region of the top electrode Li_t, not fully consumed. The white crosses are a guide to the eye for the lower part of the bottom electrode.

11

[126] prevent compositional evolution during recording. First, pure two-dimensional imaging (spatial-

[127] spatial mode) was tested, with a gradient of 175 G/cm for encoding spatially the lithium signal.

[128] Thanks to the sharp EPR lines of metallic Li (<1 G) the EPR images can be obtained with a high

[129] spatial resolution of the order of micrometers in the pristine state.[9,16]

[130]   Spatial-spatial EPR images are shown in fig. 3(left). They confirm that metallic Li is located

[131] only in the two electrodes initially (fig. 3a). The separator inside the cell, with a thickness of

[132] 500 μm, appears in the center from the absence of EPR signal during all the electrochemical steps.

[133] Its apparent size is similar to the real size and is indicative of a relatively good alignment of the

[134] cell. In principle, one would expect to observe a similar EPR intensity within the two electrodes in

[135] the pristine state. The observed contrast may have several physical origins such as, for example,

[136] local variations of the microwave field caused by shielding or eddy current effects.[9] After the

[137] positive current flow (end of polarization 1, fig. 3b), the EPR intensity decreases in electrode Li_t

[138] (top). Additional spots corresponding to metallic Li deposition appear on electrode Li_b (bottom),

[139] and more particularly at the interface with the separator. The reverse phenomenon is observed

[140] after inversion of the current flow (end of polarization 2, fig. 3c), with the metallic Li intensity

[141] increasing on the surface of Li_t, near the separator, and an intensity decrease in Li_b. This imaging

[142] mode, however, does not allow distinguishing clearly the two types of metallic Li.

[143]   In order to map the distribution of metallic lithium while preserving the spectroscopic (line-

[144] shape, resonance field) information, we turned to the correlation of spectroscopy and imaging

[145] (spectral-spatial EPR). This technique consists in scanning the whole cell with the field gradient

(175 G/cm) applied along the **Y** direction (cell axis). The image (electron density profile) is re-constructed by stacking the EPR spectra obtained for each slice along the **Y** axis. In the resulting two-dimensional plots shown in fig. 3 (right) the shape, resonance field and intensity of the EPR spectra can be determined for each slice along the **Y** cell axis. For clarity the plot indicates the variation of the absolute value of the first derivative signal $|d\chi"/dH|$ with the external magnetic field. In this representation the spectra consist in two lobes along **H** separated by a narrow domain with zero intensity. The main features of the EPR spectra can be recognized: (i) the field splitting between the two lobes gives the peak-to-peak linewidth, ΔH of the EPR line, (ii) the relative inten-sity of the two lobes gives the asymmetry ratio A/B, and (iii) the boundary between the two lobes is the value H_{res} of the external field H_0 at which resonance occurs, as indicated by dashed lines and white triangles.

The spatial distribution of the two types of lithium was obtained more precisely with these spectral-spatial images. Initially, both electrodes show similar spectral characteristics, i.e. a broad signal with the low field lobe more intense than the high field one, revealing the presence of only bulk lithium foils (fig. 3d). Several modifications are observed at the end of polarization 1 (fig 3e): (i) the EPR line is more intense in electrode Li_b than in electrode Li_t, and reveals the submicromet-ric Li deposition on the bottom electrode, in agreement with spatial-spatial imaging. Interestingly (ii) the intensity of the top (depleted) electrode is higher than in the pristine state. This effect is the consequence of the roughening of the electrode surface upon stripping (increase of the volume probed within the skin depth), in good agreement with our interpretation of pure EPR spectroscopy (fig 2b). In addition, (iii) the linewidth of bulk Li decreases in both electrodes, in agreement with

13

fig. 2c. More importantly, in fig. 3e (iv) H_{res} of the top part of the Li_b electrode is slightly shifted

to lower field (white triangle) compared to the bottom part of the same electrode (vertical dashed

line). This result indicates that the sub-micrometric particles appear at the interface with the sep-

arator and not in the bulk of the bottom electrode. This trend is magnified, though in the opposite

direction, at the end of polarization 2 (current reversed) in fig. 3f: (i) the bottom electrode is sig-

nificantly depleted, while the signal of the top electrode is narrower, more intense and symmetrical

at the interface with the separator; (ii) H_{res} of the bottom part of electrode Li_t (white triangle)

is again shifted to lower field with respect to the top part (dashed line). These features indicate

the nucleation of an increased number of sub-micrometric Li particles at the electrode-separator

interface.

Finally, let us discuss the well-known problem of dendritic lithium nucleation which ulti-

mately leads to short-circuit. Fig. 4 focuses on an *in situ* dendrite-induced short-circuit in another

symmetric Li//Li cell. This phenomenon is visible in the galvanostatic profile in fig. 4a. We de-

tected a sudden drop to 0 V after almost 38 hours of cycling with the current still flowing, which

is indicative of a global short-circuit. The corresponding evolution of the EPR intensity and A/B

of the entire spectrum are given in fig. 4b. The intensity initially increases while A/B decreases.

This indicates a progressive increase in the number of electron spins submitted to the microwave

field, a signature of sub-micrometric Li particles nucleation and of the roughening of the elec-

trodes. After the short-circuit however, the intensity no longer varies with time, in agreement with

the failure of the cell. Fig. 4c shows the EPR spectra recorded (i) in the pristine state and (ii)

after the short-circuit. The broad and asymmetric lineshape of (i) corresponds to the bulk lithium

electrodes. The second spectrum (ii) appears at lower field, symmetrical and more intense than (i) by a factor ~100. This intense and very sharp peak associated with the short-circuit corresponds to a large predominance of sub-micrometric Li particles, i.e. the modification of the morphology of the whole lithium disks. It is important to note that Li dendrites with sub-micrometric thickness may also contribute to this signal. This hypothesis is confirmed by the spatial-spatial EPR images recorded in the pristine state (fig. 4d) and after the short-circuit (fig. 4e). The presence of a dendrite is evidenced by a red spot on the right-hand side of fig. 4e that crossed the separator and short-circuited the cell. Note that the top electrode was not consumed entirely; its intensity is lower as explained above, but we can detect it (inset in fig. 4e). Additional red signals are dispersed under the bottom electrode (indicated by white crosses) and correspond to Li sub-micrometric particles deposited on the current collector after the short-circuit.

Conclusion

We performed *in situ* EPR measurements on symmetric Li/LiPF$_6$/Li cells in operating conditions. We establish *operando* EPR spectroscopy and *in situ* EPR spectral-spatial imaging as two highly complementary tools to follow the changing morphology of metallic lithium during stripping and to identify, localize and distinguish dendrites and sub-micrometric lithium particle during plating. Two main features were observed from the evolution of the EPR spectra and spectral-spatial EPR images of metallic Li in the electrochemical cell during polarization: (i) the nucleation of sub-micrometric Li particles at the interface between the separator and the electrodes; (ii) the progressive roughening of the electrodes into fragments of size slightly larger than 1 μm. We also

15

provide an *in situ* EPR image of dendrites in the separator between the two electrodes, at the origin

of a short-circuit of the electrochemical cell. To the best of our knowledge, spectral-spatial EPR

imaging was never used to investigate such electrochemical devices and we hope that these results

will pave the way to the combination of *operando* EPR spectroscopy and *in situ* spectral-spatial

EPR imaging to diagnose new generations of lithium-ion batteries.

Methods

Electrochemical cell The symmetric Li/LiPF$_6$/Li electrochemical cells were assembled in the

homemade EPR cell previously developed [6] using an argon-filled glove box. The current collectors

were copper disks on each side. The electrodes were metallic lithium disks with a typical thickness

of around 400 μm and a diameter of 5 mm. One piece of porous microfiber mat (Whatman type

GF/D) was used to separate the electrodes. The whole content of the EPR cell was soaked with

electrolyte (1 mol/L LiPF$_6$ in a mixture of ethylene and dimethyl carbonate in weight ratio 1:1,

Merck). Galvanostatic control was performed at room temperature using a VSP galvanostat from

Bio-Logic. The EPR cell was polarized (polarizations 1 and 2 in fig. 1a) with a current density

of 1 mA/cm^2. The current was paused at the end of polarization 1 to record the images. EPR

spectra were recorded continuously during polarization with a time resolution of 5 min (*operando*

EPR spectroscopy). The same procedure was used for polarization 2, with a current of -1 mA/cm^2.

The second EPR cell was polarized with a current density of 0.63 mA/cm^2 for 3 hours and -

0.63 mA/cm^2 for 3 hours. It was polarized positively again, with the same current as before,

during 20 hours to observe the nucleation of dendrites.

16

228 ***In situ* EPR** *In situ* continuous wave (cw) electron paramagnetic resonance experiments were

229 carried out using a conventional X-band Bruker E500 spectrometer operating at around 9.6 GHz

230 and room temperature. The microwave power supplied into the resonator was set to 4 mW in

231 order to avoid saturation of the EPR signal. The 100 kHz modulation depth of the magnetic field

232 was set to 0.1 mT or less to prevent distortion due to over-modulation. Conversion time and time

233 constant were set to 40.96 ms and 20.48 ms respectively. Cw-EPR spectra were fitted with one

234 dysonian and one derivative of Lorentzian using Matlab. The resonance fields of bulk (dysonian)

235 and sub-micrometric Li (Lorentzian) were fixed at 349.15 and 349.12 mT respectively.

236 The spectral-spatial and spatial-spatial images were recorded with a field-of-view of 7 mm

237 and gradient strength of 175 G/cm. The size of spatial-spatial images was 512×512 pixels re-

238 sulting in a pixel size of 13.7 μm. The high resolution spatial-spatial EPR images were obtained

239 after a deconvolution of the acquired projections under a magnetic field gradient from a signal

240 recorded without gradient and a filtered back-projection. 140 projections were recorded for the

241 spectral-spatial images with a spectral resolution of 1024 points and a pixel size of 13.7 μm in

242 the spatial dimension. The high resolution spectral-spatial images were obtained from a filtered

243 back-projection of the acquired projections.

17

1. Liu, K., Liu, Y., Lin, D., Pei, A. & Cui, Y. Materials for lithium-ion battery safety. *Science Advances* **4** (2018).

2. Waldmann, T., Hogg, B. I. & Wohlfahrt-Mehrens, M. Li plating as unwanted side reaction in commercial Li-ion cells – A review. *Journal of Power Sources* **384**, 107–124 (2018).

3. Hatzell, K. B. *et al.* Challenges in lithium metal anodes for solid-state batteries. *ACS Energy Letters* **5**, 922–934 (2020).

4. Liu, Q. *et al.* Understanding undesirable anode lithium plating issues in lithium-ion batteries. *RSC Advances* **6**, 88683–88700 (2016).

5. Foroozan, T., Sharifi-Asl, S. & Shahbazian-Yassar, R. Mechanistic understanding of li dendrites growth by in- situ/operando imaging techniques. *Journal of Power Sources* **461**, 228135 (2020).

6. Sathiya, M. *et al.* Electron paramagnetic resonance imaging for real-time monitoring of li-ion batteries. *Nature Communications* **6** (2015).

18

7. Wandt, J. *et al.* Operando electron paramagnetic resonance spectroscopy – formation of mossy lithium on lithium anodes during charge–discharge cycling. *Energy Environ. Sci.* **8**, 1358–1367 (2015).

8. Wandt, J., Jakes, P., Granwehr, J., Eichel, R.-A. & Gasteiger, H. A. Quantitative and time-resolved detection of lithium plating on graphite anodes in lithium ion batteries. *Materials Today* **21**, 231 – 240 (2018).

9. Niemöller, A., Jakes, P., Eichel, R. A. & Granwehr, J. EPR Imaging of Metallic Lithium and its Application to Dendrite Localisation in Battery Separators. *Scientific Reports* **8**, 1–7 (2018).

10. Dyson, F. J. Electron spin resonance absorption in metals. ii. theory of electron diffusion and the skin effect. *Phys. Rev.* **98**, 349–359 (1955).

11. Feher, G. & Kip, A. F. Electron spin resonance absorption in metals. i. experimental. *Phys. Rev.* **98**, 337–348 (1955).

12. Overhauser, A. W. Polarization of nuclei in metals. *Physical Review* **92**, 411–415 (1953).

13. Vigreux, C., Binet, L. & Gourier, D. Bistable Conduction Electron Spin Resonance in Metallic Lithium Particles. *The Journal of Physical Chemistry B* **102**, 1176–1181 (1998).

14. Vigreux, C., Loiseau, P., Binet, L. & Gourier, D. Anomalous metallic lithium phases: Identification by ESR, ENDOR, and the bistable Overhauser effect. *Physical Review B - Condensed Matter and Materials Physics* **61**, 8759–8770 (2000).

288   15. Hope, M. A. *et al.* Selective NMR observation of the SEI-metal interface by dynamic nuclear

289   polarisation from lithium metal. *Nature communications* **11**, 2224 (2020).

290   16. Maresch, G. G., Mehring, M. & Emid, S. High resolution ESR imaging. *Physica B+C* **138**,

291   261–263 (1986).